



# Facet-dependent reactivity of $\alpha$ -Fe<sub>2</sub>O<sub>3</sub> nanosheet on reactive oxygen species generation in Fenton-like process

Yue Yin<sup>a</sup>, Yake Zhang<sup>a</sup>, Bo Wu<sup>a</sup>, Limin Hu<sup>a</sup>, Yan Wang<sup>a</sup>, Junfeng Wan<sup>a,\*</sup>,  
Weiming Zhang<sup>b,c,d,\*\*</sup>

<sup>a</sup> School of Ecology and Environment, Zhengzhou University, Zhengzhou 450001, China

<sup>b</sup> State Key Laboratory of Pollution Control and Resource Reuse, School of the Environment, Nanjing University, Nanjing 210023, China

<sup>c</sup> Research Center for Environmental Nanotechnology (ReCENT), Nanjing University, Nanjing 210023, China

<sup>d</sup> State Environmental Protection Engineering Center for Organic Chemical Wastewater Treatment and Resource Reuse, Nanjing 210046, China

## ARTICLE INFO

### Keywords:

Iron oxides  
Nanosheet  
Exposed facets  
Fenton-like chemistry  
Water remediation

## ABSTRACT

Differences in physical structure (e.g., size, morphology, and exposed facets) will lead to divergence in the understanding of Fenton-like mechanisms. Herein, an iron oxide nanosheet predominated by (3 1 1) facet was prepared by the ultrasonic-assisted method to reveal the single factor of the catalytic descriptors. The adsorption energy of H<sub>2</sub>O<sub>2</sub> on the (3 1 1) facet was only −0.99 eV, which was lower than that on other facets such as (4 0 0) and (2 2 0). Moreover, the energy barriers for the H<sub>2</sub>O<sub>2</sub> activation on (4 0 0), (2 2 0) and (3 1 1) facets were 0.82, 0.64 and 0.30 eV, respectively. This will facilitate the adsorption and activation of H<sub>2</sub>O<sub>2</sub> on the (3 1 1) facet during hydroxyl radicals (HO•) formation. Furthermore, intermediate O<sub>2</sub><sup>•−</sup> adsorbed on the (3 1 1) facet will act as a precursor to form the first-excited-state singlet oxygen (<sup>1</sup>O<sub>2</sub>) for advanced oxidation of pollutants. Additionally, the nanosheet structure and good electrochemical properties of the Fe<sub>2</sub>O<sub>3</sub>-sheet will also facilitate electron transfer in Fe<sub>2</sub>O<sub>3</sub>-sheet/H<sub>2</sub>O<sub>2</sub> system. Overall, this study provides a comprehensive view on the relationship between exposed facets and the efficiency of H<sub>2</sub>O<sub>2</sub> activation, and optimizes the design of catalysts with high Fenton-like activity in the deep purification of wastewater.

## 1. Introduction

Hydroxyl radicals (HO•), one of the most powerful and green oxidants ( $E^0 = 2.73$  V), have been attracted extensive attention in wastewater treatment for refractory organics degradation [1–3]. Fenton chemistry has been recognized as the greenest and most efficient technology for HO• generation owing to its high reaction rate and environment-friendly reaction process [4,5]. However, the homogeneous Fenton process suffers from intrinsic bottlenecks, such as narrow working pH range and iron sludge formation, which need to be ameliorated [6,7]. In this regard, extensive studies have been focused on the heterogeneous Fenton process. But the complicated interface processes and mechanisms are still divergent, which needs to be further elucidated, especially at the level of atomic coordination [8,9].

Iron oxides (e.g.,  $\alpha$ -Fe<sub>2</sub>O<sub>3</sub>, Fe<sub>3</sub>O<sub>4</sub> and  $\alpha$ -FeOOH), as one of the most stable, environment-friendly, and cost-effective 3d transition metal oxides, are the most studied Fenton-like catalysts in recent years [10–12].

Due to the differences in physical structure (e.g., size, morphology and exposed facets), there are divergences in the understanding of Fenton-like mechanisms [13]. For instance, HO• was considered as the main reactive oxygen species (ROS) in supported Fe-Ti bimetallic oxides mediated Fenton-like process [14]. While Fe(IV)=O was identified as the main ROS in the doped Fe-Ti bimetallic oxides mediated Fenton-like process [15]. The poor structural uniformity of iron oxides leads to numerous interferences in the regulation of the chemical environment of iron sites, and the synergy mechanism between different components is still controversial [16–18]. Therefore, the single factor of the physical structure is of paramount importance to be uncovered to exploring the intrinsic mechanism of H<sub>2</sub>O<sub>2</sub> activation in the Fenton-like process.

Facets with different iron coordination forms exhibit a central role in the pathways and kinetics of H<sub>2</sub>O<sub>2</sub> activation [19]. In general, high-active facets correspond to high-index facets that are endowed with favorable atomic coordination [20]. The different coordination forms of atoms on exposed facets usually have a remarkable impact on the

\* Corresponding author.

\*\* Corresponding author at: State Key Laboratory of Pollution Control and Resource Reuse, School of the Environment, Nanjing University, Nanjing 210023, China.

E-mail addresses: [wanjunfeng@zzu.edu.cn](mailto:wanjunfeng@zzu.edu.cn) (J. Wan), [wmzhang@nju.edu.cn](mailto:wmzhang@nju.edu.cn) (W. Zhang).

catalytic activity [21]. For instance, the most favorable configuration between  $\text{H}_2\text{O}_2$  and  $\text{CuFeO}_2$  (0 1 2) facet was formed with a larger O–O bond length (3.290 Å) than that on (1 1 0) facet (1.468 Å), which favors the  $\text{H}_2\text{O}_2$  activation and  $\text{HO}^\bullet$  formation owing to the more feasible electron transfer process [22]. Moreover, in hematite mediated Fenton-like process, iron cations on the (0 0 1) facet mainly existed in the valence state of Fe(III), and primarily showed an oxidation state between Fe(III) and Fe(II) on (1 0 4) and (1 1 3) facets [23]. The low valence state of iron will also facilitate  $\text{H}_2\text{O}_2$  activation to generation more  $\text{HO}^\bullet$ . It can be inferred that the  $\text{H}_2\text{O}_2$  adsorption, activation, and  $\text{HO}^\bullet$  transformation may be determined by chemical environment of iron sites closely relating to the atomic arrangement over the catalyst facets. However, due to the difference in the proportion of each facet in iron oxides, there are still a lack of the structure-performance relationships between the chemical environment of iron sites on different facets and the performance of  $\text{H}_2\text{O}_2$  activation in Fenton-like process.

Therefore, the aim of this research was to reveal the facet-dependent effects of  $\text{H}_2\text{O}_2$  activation on the common iron sites. Herein,  $\alpha\text{-Fe}_2\text{O}_3$  nanosheets were obtained by ultrasonic assistance, with predominant (3 1 1) facet, to reduce the interference of other structural features. Factors such as pore size, surface hydroxyl and oxygen vacancies were normalized to reveal the intrinsic impact of the facets on the catalytic descriptors. The mechanism of  $\text{H}_2\text{O}_2$  activation on different iron oxides facets were investigated. And the relationship between chemical environment of iron sites and ROS generation were established. Significantly, the results will also rationalize the design of catalysts with high Fenton-like activity in environmental remediation.

## 2. Experiments

### 2.1. Chemicals and reagents

All chemicals were analytical grade and used without further purification (Supporting Information, SI, Text S1).

### 2.2. Catalysts preparation

$\text{Fe}_2\text{O}_3$ : Dropping 1.0 mol  $\text{L}^{-1}$   $\text{NH}_4\text{OH}$  solution into 20 mL 1.0 mol  $\text{L}^{-1}$   $\text{FeCl}_3$  solution at a rate of 0.1 mL  $\text{min}^{-1}$  until the pH of the solution reached  $7.0 \pm 0.1$ . The suspension was aged for 60 min. And washed the obtained nanoparticles with deionized water until the pH of the effluent reached  $7.0 \pm 0.1$ .

$\text{Fe}_2\text{O}_3$ -sheet: Dropping 1.0 mol  $\text{L}^{-1}$   $\text{NH}_4\text{OH}$  solution into 20 mL 1.0 mol  $\text{L}^{-1}$   $\text{FeCl}_3$  solution at a rate of 0.1 mL  $\text{min}^{-1}$  until the pH of the solution reached  $7.0 \pm 0.1$ . The solid was added into the acetonitrile solution ( $V_{\text{acetonitrile}}: V_{\text{water}} = 40: 60$ ). And ultrasonic oscillation at 650 W in ice bath for 20 min (ultrasonic oscillation 1 s, interval 1 s). The obtained nanosheets were washed with deionized water until the pH of the effluent reached  $7.0 \pm 0.1$ .

### 2.3. Characterization

Structure and composition of these catalysts were performed by SEM, TEM, XRD,  $\text{N}_2$  adsorption-desorption instrument, TGA, FTIR, XPS and Mössbauer spectroscopy, respectively. Fe K-edge synchrotron X-ray absorption spectroscopy of these catalysts were collected at 1W1B beamline of Beijing Synchrotron Radiation Facility (Beijing, China).

### 2.4. Experimental procedure

Bisphenol A (BPA) was selected as the model pollutant to evaluate the activity of the catalysts. The typical experimental suspension (100 mL) contained 0.5 g  $\text{L}^{-1}$  catalysts, 10 mM  $\text{H}_2\text{O}_2$  and 0.1 mM BPA in a brown reaction flask with constant stirring. And samples were filtrated by 0.22  $\mu\text{m}$  filter and terminated the reaction by 0.1 M  $\text{Na}_2\text{S}_2\text{O}_3$ .

Terephthalic acid (TA, 20 mM) was selected as probe to quantify the

steady state of  $\text{HO}^\bullet$ . The generation of superoxide anion ( $\text{O}_2^{\bullet-}$ ) was semi-quantitative by nitro blue tetrazolium (NBT) method. The 2,2,6,6-tetramethylpiperidinyloxy (TEMP) was used as singlet oxygen ( $^1\text{O}_2$ ) trapping agent, detected by ESR spectrometer without BPA addition. And the contribution of  $^1\text{O}_2$  to BPA degradation was calculated as follows:

$$k_{\text{obs}, \text{H}_2\text{O}, \text{D}_2\text{O}} = \frac{k_{\text{H}_2\text{O}} \bullet k_{\text{obs}, \text{H}_2\text{O}}}{x_{\text{H}_2\text{O}} \bullet k_{\text{H}_2\text{O}} + x_{\text{D}_2\text{O}} \bullet k_{\text{D}_2\text{O}}} \quad (1)$$

where  $x_{\text{H}_2\text{O}}$  and  $x_{\text{D}_2\text{O}}$  represent the molar fraction of  $\text{H}_2\text{O}$  and  $\text{D}_2\text{O}$ , respectively.  $k_{\text{obs}, \text{H}_2\text{O}}$  is rate constant of BPA degradation in 100 %  $\text{H}_2\text{O}$ .  $k_{\text{H}_2\text{O}}$  and  $k_{\text{D}_2\text{O}}$  are  $2.5 \times 10^5 \text{ M}^{-1} \text{ s}^{-1}$  and  $1.6 \times 10^4 \text{ M}^{-1} \text{ s}^{-1}$ , respectively [24]. And the experiments were carried out in a mixed solution of 20 %  $\text{H}_2\text{O}$  and 80 %  $\text{D}_2\text{O}$ .

Parallel experiments were also conducted. And all detailed instrument conditions are given in Text S2.

### 2.5. Theoretical calculation

DFT calculations were adopted to use the Vienna Ab initio Simulation Package (VASP) [25]. The projector augmented wave pseudopotential and the generalized gradient approximation were parameterized for exchange correlation function [26,27]. All energetics of metal oxides were calculated by DFT+U to account for strongly localized d-electrons for Fe with  $U_{\text{eff}}(\text{Fe}) = 5.3 \text{ eV}$  [28]. The cut-off energy of the plane waves basis set was 500 eV, and a Monkhorst-Pack mesh of  $k$  point was sampled by  $3 \times 3 \times 1$ . All structures were spin-polarized, and all atoms were fully relaxed with the final force on each atom was  $< 0.01 \text{ eV } \text{\AA}^{-1}$ .

## 3. Results and discussions

### 3.1. Analysis of catalysts structure

As depict in high resolution SEM and TEM images, iron oxides synthesized by the precipitation method exhibited a stacked nanoparticle morphology with diameter of  $41.5 \pm 6.3 \text{ nm}$  (Fig. 1a and S1), while that synthesized by the ultrasonic-assisted method presented a dispersed nanosheet morphology with  $(125.5 \pm 34.9) \times (38.6 \pm 12.1) \text{ nm}$  (Fig. 1d). According to the Fe K-edge XANES spectra, the absorption thresholds of the two kind of iron oxides were both close to  $\alpha\text{-Fe}_2\text{O}_3$  (Fig. 1c). But the exposed facets were significantly different. The (2 2 0), (3 1 1) and (4 0 0) facets with interplanar spacing of 2.95 Å, 2.52 Å and 2.09 Å were clearly observed in  $\text{Fe}_2\text{O}_3$  (Fig. 1b), corresponding to the characteristic diffraction peaks at  $30.2^\circ$ ,  $35.6^\circ$  and  $43.3^\circ$  of the XRD pattern (Fig. 1f). Strikingly, a significant characteristic diffraction peak was detected at  $35.6^\circ$  in  $\text{Fe}_2\text{O}_3$ -sheet, which corresponds to the (3 1 1) facet (Fig. 1e). And the peak area ratios at  $35.6^\circ$  and  $30.2^\circ$  increased from 2.9 for  $\text{Fe}_2\text{O}_3$  to 6.2 for  $\text{Fe}_2\text{O}_3$ -sheet. This indicates that a nanosheet iron oxide dominated by the (3 1 1) facet was prepared by the ultrasonic-assisted method.

Moreover, absorbance bands attributed to the surface -OH vibration of  $\nu(\text{-OH})$  at  $1075 \text{ cm}^{-1}$  was enhanced in  $\text{Fe}_2\text{O}_3$ -sheet (Fig. S2). It can be concluded that, in addition to the (3 1 1) facet with oriented growth, there are more -OH on  $\text{Fe}_2\text{O}_3$ -sheet surface than  $\text{Fe}_2\text{O}_3$ . Significantly, -OH may directly activate  $\text{H}_2\text{O}_2$  through electron transfer process in  $\text{d}^0$  orbitals (non-Fenton pathway) [29]. It means that a large amount of -OH on the  $\text{Fe}_2\text{O}_3$ -sheet surface will hinder the identification of the single descriptor of the catalysts structure. So, the  $\text{Fe}_2\text{O}_3$  and  $\text{Fe}_2\text{O}_3$ -sheet were then calcined at  $400^\circ\text{C}$  in a nitrogen atmosphere to remove the surface -OH (Fig. S3a), without changing the crystal structure of the two catalysts (Fig. S3b). And the calcined materials were used in subsequent experiments.

Furthermore, volume to surface ratio (VSR) was introduced to normalize the pore volume and specific surface area data obtained by nitrogen adsorption-desorption isotherms (Fig. S4). A relatively constant VSR corresponding to  $\text{Fe}_2\text{O}_3$  and  $\text{Fe}_2\text{O}_3$ -sheet were  $5.85 \times 10^{-3}$  and

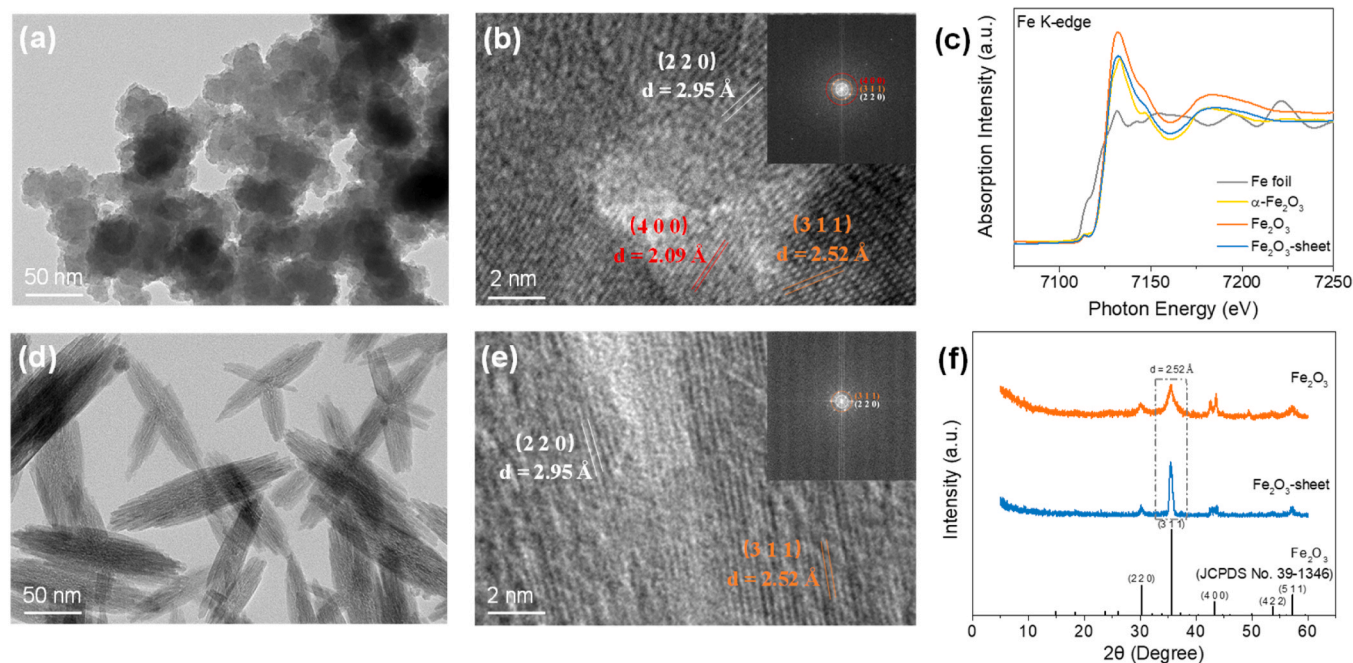


Fig. 1. HRTEM images of (a), (b) Fe<sub>2</sub>O<sub>3</sub> and (d), (e) Fe<sub>2</sub>O<sub>3</sub>-sheet; (c) Iron K-edge XANES spectra and (f) XRD patterns of Fe<sub>2</sub>O<sub>3</sub> and Fe<sub>2</sub>O<sub>3</sub>-sheet.

$5.76 \times 10^{-3}$ , respectively, which implies that the impact of surface availability to drive chemical reaction in the bulk phase (*i.e.*, aqueous solution inside the pore) will remain relatively constant and all catalytic sites equally contribute to the activity [30].

### 3.2. Difference in H<sub>2</sub>O<sub>2</sub> activation by catalysts

#### 3.2.1. BPA degradation

First of all, the removal rate of BPA by adsorption in both Fe<sub>2</sub>O<sub>3</sub>/H<sub>2</sub>O<sub>2</sub> and Fe<sub>2</sub>O<sub>3</sub>-sheet/H<sub>2</sub>O<sub>2</sub> systems was less than 4 % after 24 h

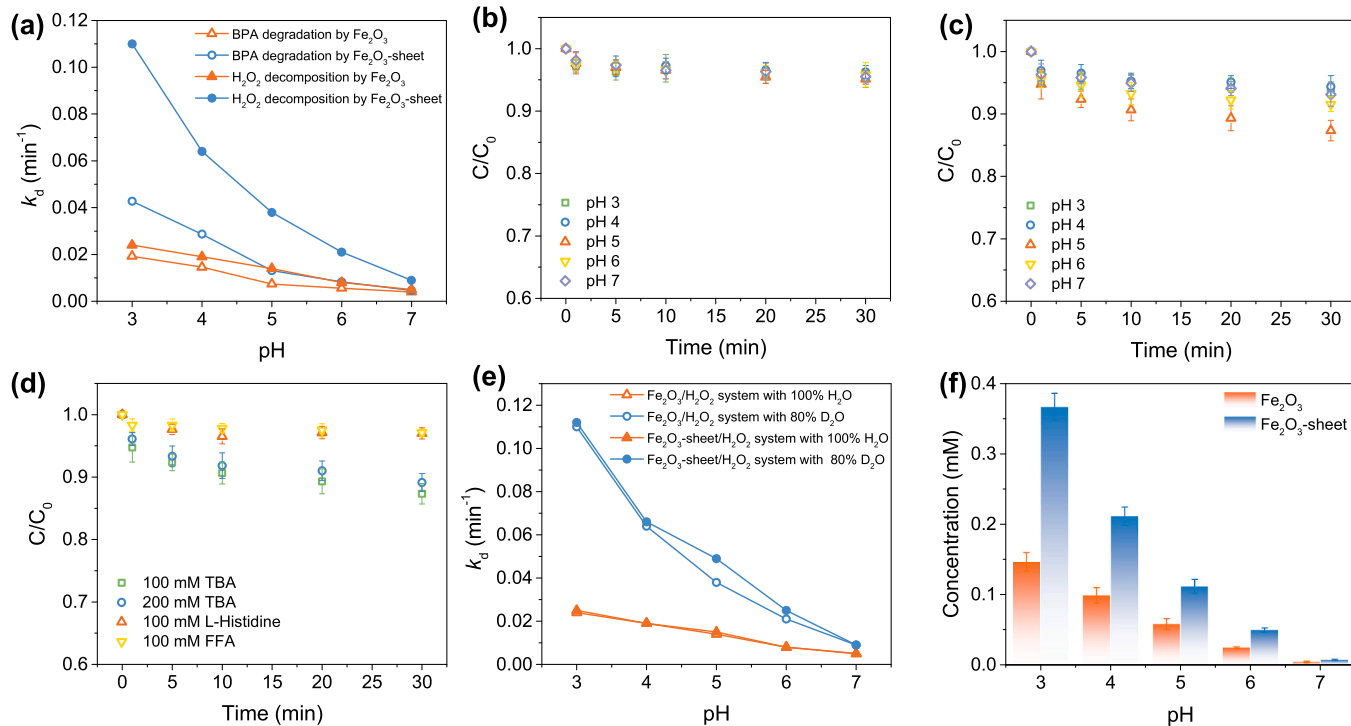


Fig. 2. (a) Pseudo-first-order rate constant of BPA degradation and H<sub>2</sub>O<sub>2</sub> decomposition in Fe<sub>2</sub>O<sub>3</sub>/H<sub>2</sub>O<sub>2</sub> and Fe<sub>2</sub>O<sub>3</sub>-sheet/H<sub>2</sub>O<sub>2</sub> systems at different pH value (Catalyst dosage = 0.5 g L<sup>-1</sup>, [H<sub>2</sub>O<sub>2</sub>]<sub>0</sub> = 10 mM, [BPA]<sub>0</sub> = 0.1 mM); HO<sup>•</sup> quenching experiments in (b) Fe<sub>2</sub>O<sub>3</sub>/H<sub>2</sub>O<sub>2</sub> and (c) Fe<sub>2</sub>O<sub>3</sub>-sheet/H<sub>2</sub>O<sub>2</sub> systems (Catalyst dosage = 0.5 g L<sup>-1</sup>, [H<sub>2</sub>O<sub>2</sub>]<sub>0</sub> = 10 mM, [BPA]<sub>0</sub> = 0.1 mM, [TBA]<sub>0</sub> = 100.0 mM); (d) BPA degradation in Fe<sub>2</sub>O<sub>3</sub>-sheet/H<sub>2</sub>O<sub>2</sub> system under different conditions (Catalyst dosage = 0.5 g L<sup>-1</sup>, [H<sub>2</sub>O<sub>2</sub>]<sub>0</sub> = 10 mM, [BPA]<sub>0</sub> = 0.1 mM, [TBA]<sub>0</sub> = 100.0 mM and 200.0 mM, [L-histidine]<sub>0</sub> = 100.0 mM, [FFA]<sub>0</sub> = 100.0 mM, pH = 5.0 ± 0.1); (e) kinetic solvent isotopic effect in Fe<sub>2</sub>O<sub>3</sub>/H<sub>2</sub>O<sub>2</sub> and Fe<sub>2</sub>O<sub>3</sub>-sheet/H<sub>2</sub>O<sub>2</sub> systems (Catalyst dosage = 0.5 g L<sup>-1</sup>, [H<sub>2</sub>O<sub>2</sub>]<sub>0</sub> = 10 mM, [BPA]<sub>0</sub> = 0.1 mM, pH = 5.0 ± 0.1); (f) concentration of steady state of HO<sup>•</sup> in Fe<sub>2</sub>O<sub>3</sub>/H<sub>2</sub>O<sub>2</sub> and Fe<sub>2</sub>O<sub>3</sub>-sheet/H<sub>2</sub>O<sub>2</sub> systems during 30 min (Catalyst dosage = 0.5 g L<sup>-1</sup>, [H<sub>2</sub>O<sub>2</sub>]<sub>0</sub> = 10 mM, [TA]<sub>0</sub> = 20.0 mM).



(Fig. S5), which means that adsorption process had a negligible effect on BPA removal compared to the catalytic degradation process. The rate appearing to be pseudo-first-order rate constant of BPA degradation ( $k_{d, \text{BPA}}$ ) under different conditions as described in  $\ln([BPA]_t/[BPA]_0) = -k_{d, \text{BPA}} \cdot t$ . The  $k_{d, \text{BPA}}$  value in  $\text{Fe}_2\text{O}_3/\text{H}_2\text{O}_2$  and  $\text{Fe}_2\text{O}_3\text{-sheet}/\text{H}_2\text{O}_2$  systems were both showing a downward trend with the increase of the pH value (Fig. S6). But the  $k_{d, \text{BPA}}$  in the  $\text{Fe}_2\text{O}_3\text{-sheet}/\text{H}_2\text{O}_2$  system was always higher than that in the  $\text{Fe}_2\text{O}_3/\text{H}_2\text{O}_2$  system under the same pH conditions. And the  $k_{d, \text{BPA}}$  was almost 4.6 times higher than that in  $\text{Fe}_2\text{O}_3/\text{H}_2\text{O}_2$  system at  $\text{pH } 3.0 \pm 0.1$  (Fig. 2a). Moreover, the degradation rate of BPA in the  $\text{Fe}_2\text{O}_3/\text{H}_2\text{O}_2$  system was only 53.6 % within 30 min, while that in the  $\text{Fe}_2\text{O}_3\text{-sheet}/\text{H}_2\text{O}_2$  system was reached 96.5 % at  $\text{pH } 3.0 \pm 0.1$ . Besides, it is noteworthy that the rate constant of  $\text{H}_2\text{O}_2$  decomposition ( $k_{d, \text{H}_2\text{O}_2}$ ) in  $\text{Fe}_2\text{O}_3\text{-sheet}/\text{H}_2\text{O}_2$  system was much higher than that in  $\text{Fe}_2\text{O}_3/\text{H}_2\text{O}_2$  system especially under acidic conditions (Fig. 2a and S7). This indicates that the  $\text{Fe}_2\text{O}_3\text{-sheet}$  may exhibit a stronger  $\text{H}_2\text{O}_2$  activation ability than  $\text{Fe}_2\text{O}_3$ .

### 3.2.2. ROS identification

In order to further evaluate the performance of  $\text{H}_2\text{O}_2$  activation by  $\text{Fe}_2\text{O}_3$  and  $\text{Fe}_2\text{O}_3\text{-sheet}$ , the formation of ROS in  $\text{Fe}_2\text{O}_3/\text{H}_2\text{O}_2$  and  $\text{Fe}_2\text{O}_3\text{-sheet}/\text{H}_2\text{O}_2$  systems was then identified. Excessive tert-butyl alcohol (TBA) was used to quench  $\text{HO}^\bullet$ , owing to the high reaction rate constant between TBA and  $\text{HO}^\bullet$  ( $k_{\text{HO}^\bullet, \text{TBA}} = 6.0 \times 10^8 \text{ M}^{-1} \text{ s}^{-1}$ ) [31]. As shown in Fig. 2b, the degradation of BPA in  $\text{Fe}_2\text{O}_3/\text{H}_2\text{O}_2$  system was almost completely inhibited after 100 mM TBA addition. It means that  $\text{HO}^\bullet$  was the main ROS for BPA oxidation in the  $\text{Fe}_2\text{O}_3/\text{H}_2\text{O}_2$  system. Notably, TBA could not completely inhibit BPA degradation in  $\text{Fe}_2\text{O}_3\text{-sheet}/\text{H}_2\text{O}_2$  system especially at  $\text{pH } 5.0 \pm 0.1$  (Fig. 2c), which the degradation efficiency of BPA was still 12.7 %. Moreover, when the concentration of TBA was increased to 200 mM, the degradation efficiency of BPA in the  $\text{Fe}_2\text{O}_3\text{-sheet}/\text{H}_2\text{O}_2$  system remained at 10.9 %. This suggests that there may be other ROS in the  $\text{Fe}_2\text{O}_3\text{-sheet}/\text{H}_2\text{O}_2$  system that can degrade BPA, especially at  $\text{pH } 5.0 \pm 0.1$ .

High-valent iron oxo species and  $^1\text{O}_2$  are also generally considered to be the ROS generated under near-neutral conditions [32,33]. Firstly, 1 mM methyl phenyl sulfoxide (PMSO) was selected as a probe to identify the high-valent iron oxo species generated in the  $\text{Fe}_2\text{O}_3\text{-sheet}/\text{H}_2\text{O}_2$  system, owing to the unique oxygen product methyl phenyl sulfone (PMSO<sub>2</sub>) formation [34]. As can be seen from the Fig. S8, there was only hydroxylated PMSO detected in the system rather than high-valent iron oxo species derived product PMSO<sub>2</sub>. Thus, it is suggested that there was no high-valent iron oxo species formation in  $\text{Fe}_2\text{O}_3\text{-sheet}/\text{H}_2\text{O}_2$  system.

Furthermore, compared with the lower reaction rate between TBA and  $^1\text{O}_2$  ( $k_{\text{TBA}, ^1\text{O}_2} = 1.8 \times 10^3 \text{ M}^{-1} \text{ s}^{-1}$ ), the rate constants  $k_{\text{FFA}, ^1\text{O}_2}$  and  $k_{\text{L-histidine}, ^1\text{O}_2}$  are as high as  $1.2 \times 10^8$  and  $1.5 \times 10^8 \text{ M}^{-1} \text{ s}^{-1}$ , respectively, which means furfuryl alcohol (FFA) and L-histidine are able to quench  $\text{HO}^\bullet$  and  $^1\text{O}_2$  in the system simultaneously [35]. As depict in Fig. 2d, the BPA degradation in  $\text{Fe}_2\text{O}_3\text{-sheet}/\text{H}_2\text{O}_2$  system was almost completely inhibited at  $\text{pH } 5.0 \pm 0.1$  after 100 mM FFA or L-histidine addition. It is inferred that  $^1\text{O}_2$  in  $\text{Fe}_2\text{O}_3\text{-sheet}/\text{H}_2\text{O}_2$  system may be involved in the degradation of BPA. 1,3-diphenylisobenzofuran (DPBF) was then used as the  $^1\text{O}_2$  scavenger [36], and the unique oxidized product of 1,2-dibenzoylbenzene was detected at 410 nm in  $\text{Fe}_2\text{O}_3\text{-sheet}/\text{H}_2\text{O}_2$  system (Fig. S9). It means that  $^1\text{O}_2$  was actually involved in the BPA degradation. Thereafter, the contribution of BPA degradation by  $^1\text{O}_2$  was further validated and quantified according to the kinetic solvent isotopic effect (KSIE). The quenching rate constants for  $^1\text{O}_2$  by  $\text{H}_2\text{O}$  and  $\text{D}_2\text{O}$  were determined to be  $2.5 \times 10^5 \text{ M}^{-1} \text{ s}^{-1}$  and  $1.6 \times 10^4 \text{ M}^{-1} \text{ s}^{-1}$ , respectively [37]. It means the  $^1\text{O}_2$  induced reactions is approximately 15.6 times slower in pure  $\text{D}_2\text{O}$  than that in pure  $\text{H}_2\text{O}$ . The  $k_{d, \text{BPA}}$  in 100 %  $\text{H}_2\text{O}$  were determined to be  $0.038 \text{ min}^{-1}$  (Fig. 2e). According to Eq. 1, if the BPA degradation was only attributed to  $^1\text{O}_2$ , the  $k_{d, \text{BPA}}$  in 80 %  $\text{D}_2\text{O}$  was  $0.151 \text{ s}^{-1}$ , supposing  $\text{HO}^\bullet$  does not show a KSIE. However, this

value was determined to be only  $0.049 \text{ s}^{-1}$ . Therefore, it can be calculated that  $^1\text{O}_2$  contributed around 9.7 % of the total BPA degradation in the  $\text{Fe}_2\text{O}_3\text{-sheet}/\text{H}_2\text{O}_2$  system at  $\text{pH } 5.0 \pm 0.1$ , which is in line with the results obtained by the quenching experiments (Fig. 2d). Additionally, it is demonstrated that  $^1\text{O}_2$  was involved in the BPA degradation, but  $\text{HO}^\bullet$  was still the main ROS generated in the  $\text{Fe}_2\text{O}_3\text{-sheet}/\text{H}_2\text{O}_2$  system. And the concentration of  $\text{HO}^\bullet$  in the  $\text{Fe}_2\text{O}_3\text{-sheet}/\text{H}_2\text{O}_2$  system was always higher than that in the  $\text{Fe}_2\text{O}_3/\text{H}_2\text{O}_2$  system (Fig. 2f).

### 3.3. Structure-performance relationships between catalysts structure and ROS formation

#### 3.3.1. Pathway of $^1\text{O}_2$ generation

According to the Haber-Weiss mechanism,  $\text{H}_2\text{O}_2$  participates in the internal coordination with  $\equiv\text{Fe}(\text{II})$  [38,39], forming  $\equiv\text{Fe}(\text{II})(\text{H}_2\text{O})_5(\text{H}_2\text{O}_2)_n$  through surface complexation of  $\text{H}_2\text{O}_2$  and iron oxides [40]. And changes in the chemical environment of the iron sites at the interface will influence the ROS generation in the Fenton-like system [41]. Structural features such as oxygen vacancies (OVs) on high-energy facet are capable of activating O-O bond to form  $^1\text{O}_2$  ( $1\Delta\text{g}$ ,  $92 \text{ kJ mol}^{-1}$ ) under alkaline conditions, which is generally considered to be one of the main pathways for  $^1\text{O}_2$  formation [42]. However, according to the EPR spectra of the OVs in  $\text{Fe}_2\text{O}_3$  and  $\text{Fe}_2\text{O}_3\text{-sheet}$  (Fig. S10), there were no difference in the signal intensities of the OVs at  $g = 2.002$ . Moreover, the absorbed  $\text{O}_2$  at OVs in  $\text{Fe}_2\text{O}_3$  and  $\text{Fe}_2\text{O}_3\text{-sheet}$  is almost the same (Fig. S11), and the removal of  $\text{O}_2$  did not significantly change the generation of  $^1\text{O}_2$  in the  $\text{Fe}_2\text{O}_3\text{-sheet}/\text{H}_2\text{O}_2$  system (Fig. S12). It is demonstrated that the formation of  $^1\text{O}_2$  in the  $\text{Fe}_2\text{O}_3\text{-sheet}/\text{H}_2\text{O}_2$  system was not caused by the OVs [43,44].

On the other hand,  $\text{O}_2^\bullet$  is usually regarded as the precursor of  $^1\text{O}_2$ , corresponding to another pathway of  $^1\text{O}_2$  generation. The  $\text{O}_2^\bullet$  is formed by deprotonation of  $\text{HO}_2^\bullet$  when the pH value higher than 4.8 [45]. And NBT was then selected as a semiquantitative indicator of  $\text{O}_2^\bullet$ , as it could be reduced by  $\text{O}_2^\bullet$  ( $k = 5.88 \times 10^4 \text{ M}^{-1} \text{ s}^{-1}$ ) and transformed to monoformazan [46]. The results show that there were a large amount of  $\text{O}_2^\bullet$  formed in  $\text{Fe}_2\text{O}_3\text{-sheet}/\text{H}_2\text{O}_2$  system at  $\text{pH } 5.0 \pm 0.1$  (Fig. 3a), which was consistent with the trend of  $^1\text{O}_2$  generation in the KSIE and EPR experiments (Figs. 2e and 3b).

The adsorption energy of  $\text{O}_2^\bullet$  was then calculated by the following Equation:

$$\Delta G_{\text{ads}} = \Delta E + \Delta E_{\text{ZPE}} - T\Delta S \quad (2)$$

Where  $\Delta E$  is the binding energy,  $\Delta E_{\text{ZPE}}$  is the zero-point energy change and  $\Delta S$  is the entropy change. The adsorption energy of  $\text{O}_2^\bullet$  on the (3 1 1) facet was only  $-0.24 \text{ eV}$ , which was much lower than the 0.46 and 0.65 of the (4 0 0) and (2 2 0) facets (Fig. 3c). And the negative  $\Delta G_{\text{ads}}$  means the  $\text{O}_2^\bullet$  can spontaneously adsorb on the (3 1 1) facet. Additionally, the changes in the Gibbs free energy of  $\text{O}_2^\bullet$  generation on the (4 0 0), (2 2 0) and (3 1 1) facets show that the energy barrier to be overcome to form the transition state  $\text{Fe-O-O}^\bullet$  in the pathway of  $\text{O}_2^\bullet$  generation was only  $0.46 \text{ eV}$  (Fig. 3d). When the spin polarization was considered in the calculation process, singlet oxygen tends to exist stably on the (3 1 1) facet than triplet oxygen. Moreover, the length of Fe-O bond in the transition state  $\text{Fe-O-O}^\bullet$  on the (3 1 1) facet was longer than that on (4 0 0) and (2 2 0) facets (Fig. S13), which will facilitate the generation and dissociation of low-excited-state  $^1\text{O}_2$  ( $1\Delta\text{g}$ ,  $92 \text{ kJ mol}^{-1}$ ).

#### 3.3.2. Effect of exposed facets

Difference in the exposed facets of iron oxides have changed the coordination form of iron sites, which will further influence the  $\text{H}_2\text{O}_2$  activation by iron oxides [47]. And the results have demonstrated that iron sites on the (3 1 1) facet were more favorable for the generation of  $^1\text{O}_2$ . So, in order to identify the structure-performance relationships between catalysts structure and ROS formation, the difference in the chemical environment of iron in the catalysts was then analyzed.

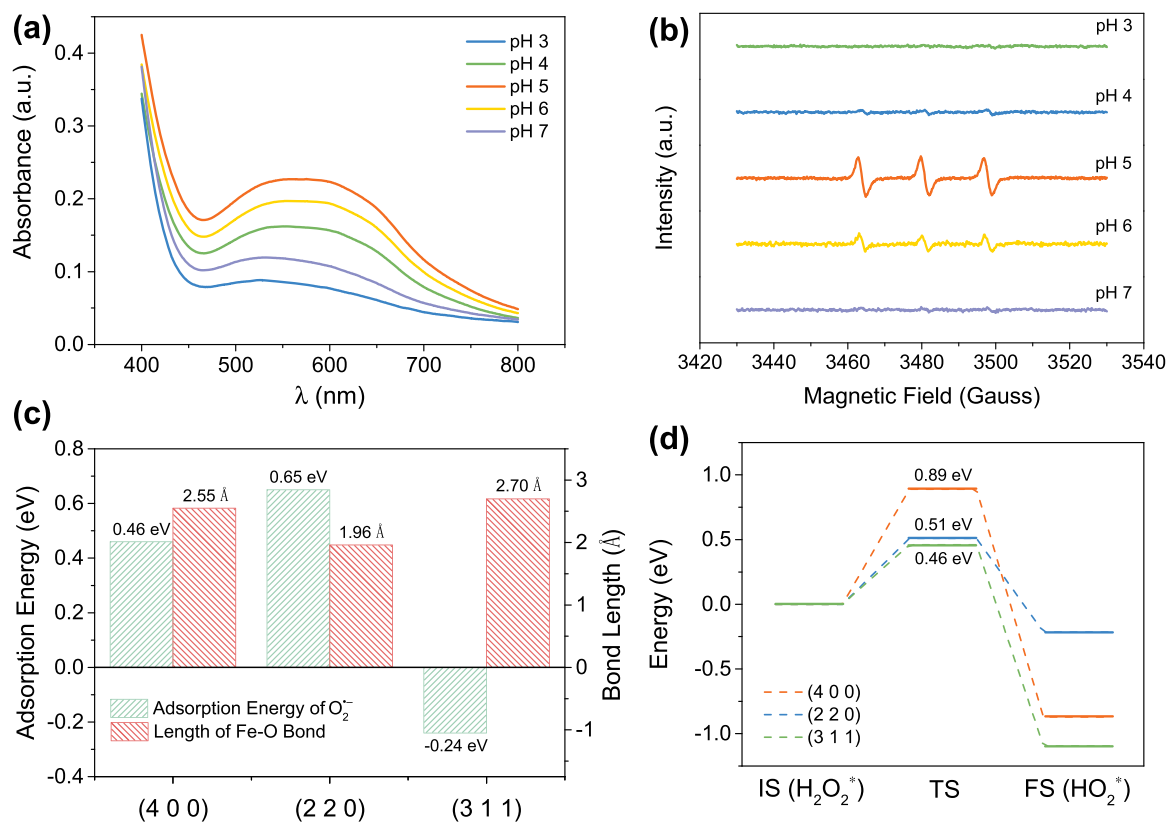


**Fig. 3.** (a) UV-vis adsorption spectra of monoformazan in  $\text{Fe}_2\text{O}_3$ -sheet/ $\text{H}_2\text{O}_2$  system. (Catalyst dosage =  $0.5 \text{ g L}^{-1}$ ,  $[\text{H}_2\text{O}_2]_0 = 10 \text{ mM}$ ,  $[\text{NBT}]_0 = 2.0 \text{ mM}$ ); (b) EPR spectra of TEMP adducts in  $\text{Fe}_2\text{O}_3$ -sheet/ $\text{H}_2\text{O}_2$  system (Catalyst dosage =  $0.5 \text{ g L}^{-1}$ ,  $[\text{H}_2\text{O}_2]_0 = 10 \text{ mM}$ ,  $[\text{TEMP}]_0 = 100 \text{ mM}$ ); (c) adsorption energies of  $\text{O}_2^*$  and length of Fe-O bond on (4 0 0), (2 2 0) and (3 1 1) facets; (d) reaction pathways of  $\text{HO}_2^*$  formation on (4 0 0), (2 2 0) and (3 1 1) facets.

$^{57}\text{Fe}$  Mössbauer spectra of the  $\text{Fe}_2\text{O}_3$  and  $\text{Fe}_2\text{O}_3$ -sheet revealed the hyperfine structure of iron sites in the catalysts. The prominent sextet corresponds to the six-coordinated iron sites in  $\alpha\text{-Fe}_2\text{O}_3$  (Fig. 4a), which was in line with the results obtained by XANES [48]. The doublet reflects the local electron distribution of Fe 3d orbitals. And the proportion of the doublet increased from 23.27 % for  $\text{Fe}_2\text{O}_3$  to 61.25 % for  $\text{Fe}_2\text{O}_3$ -sheet after ultrasonic oscillation, indicating that recoilless resonance absorption of  $^{57}\text{Fe}$   $\gamma$ -ray was enhanced. Moreover, the enhancement of the resonance absorption of the doublet suggests that the length of the  $\text{Fe}^{\text{III}}\text{Fe}$  or Fe-O bonds were shortened, and the local electron density of the Fe 3d orbitals was increased. This corresponds to the decrease in the ratio of (2 2 0) and (3 1 1) facets in the XRD pattern, and the shortening of interplanar spacing (Fig. 1f). Furthermore, the increase of the electron

density in the core layer will lead to the enhancement of the repulsion between orbital electrons, resulting in easier excitation of valence electrons. As shown in the XPS spectra (Fig. 4b), the proportion of Fe(II) in  $2p_{3/2}$  orbitals increased by 15.3 %, and the binding energy decreased by 0.41 eV. In addition, isomer shift (I. S.) of the doublet in  $\text{Fe}_2\text{O}_3$ -sheet increased by  $0.21 \text{ mm s}^{-1}$ . These structural features will be conducive to the single-electron transfer process of iron oxides and  $\text{H}_2\text{O}_2$  during the Haber-Weiss process [49].

Furthermore, the Fourier transform of the EXAFS data shows that the length of Fe-O bond in the outer shell of  $\text{Fe}_2\text{O}_3$ -sheet was  $0.15 \text{ \AA}$  shorter than that of  $\text{Fe}_2\text{O}_3$  (Fig. 5a). This will lead to an increase in the charge density around the Fe atom and promote the single-electron transfer process of peroxy bond cleavage in the transition state  $\text{Fe-O-O}^*$  [50],

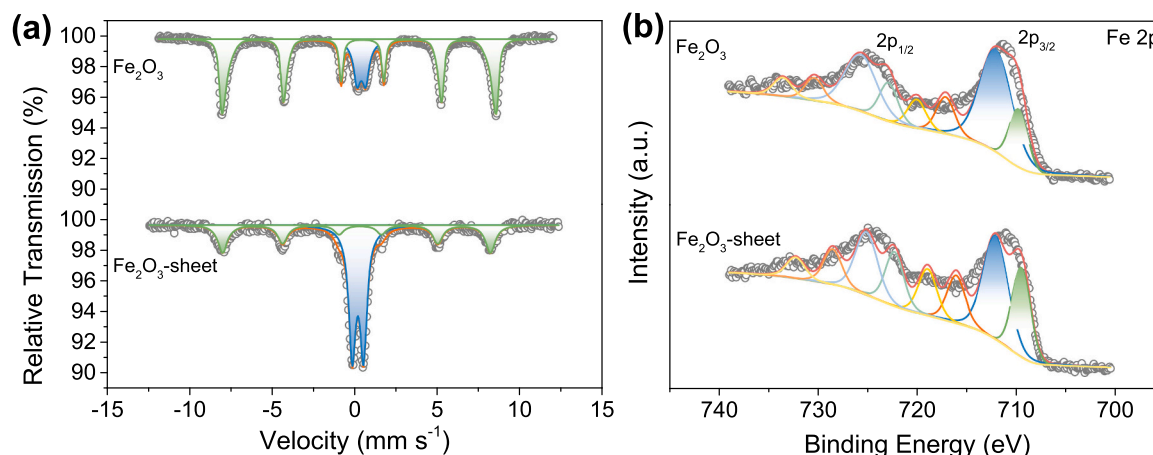


**Fig. 4.** (a) Mössbauer and (b) XPS spectra of  $\text{Fe}_2\text{O}_3$  and  $\text{Fe}_2\text{O}_3$ -sheet.

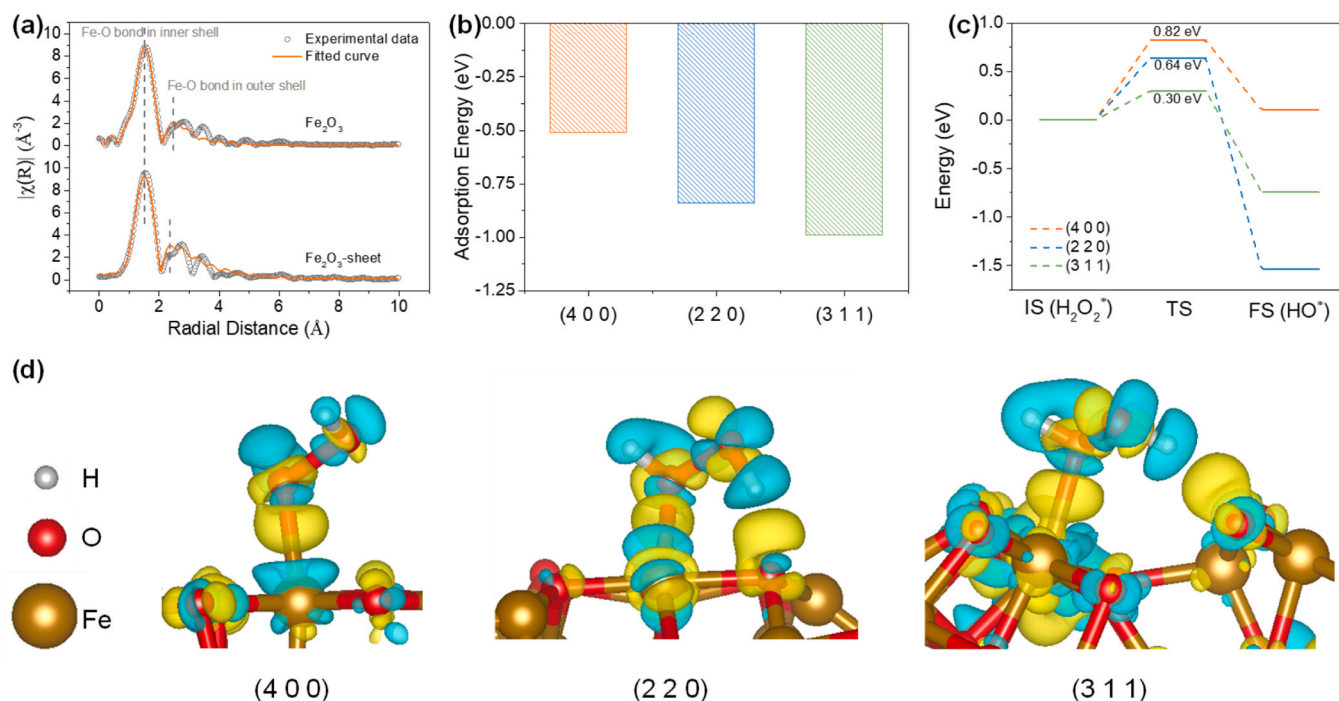


**Fig. 5.** (a) FT-EXAFS and its fitting curve of iron for  $\text{Fe}_2\text{O}_3$  and  $\text{Fe}_2\text{O}_3$ -sheet; (b) adsorption energies of  $\text{H}_2\text{O}_2$ , (c) reaction pathways of  $\text{HO}^*$  formation and (d) charge density difference of  $\text{H}_2\text{O}_2$  bonded on (4 0 0), (2 2 0) and (3 1 1) facets.

which strengthened the generation of  $\text{HO}^*$ . To further distinguish the difference of  $\text{H}_2\text{O}_2$  activation on these facets, the transition state model during  $\text{H}_2\text{O}_2$  activation on the (4 0 0), (2 2 0) and (3 1 1) facets were constructed based on the results of the previous structural characterization. The adsorption energy of  $\text{H}_2\text{O}_2$  on the (4 0 0), (2 2 0) and (3 1 1) facets were  $-0.51$ ,  $-0.84$  and  $-0.99$  eV, respectively (Fig. 5b). Moreover, as depict in the change of Gibbs free energy (Fig. 5c), the energy barriers for  $\text{H}_2\text{O}_2$  activation on the (4 0 0), (2 2 0) and (3 1 1) facets were  $0.82$ ,  $0.64$  and  $0.30$  eV, respectively. It means that  $\text{H}_2\text{O}_2$  was more inclined to adsorb on the (3 1 1) facet, and the activation energy on the (3 1 1) facet was much lower than that on the (4 0 0) and (2 2 0) facets during the  $\text{HO}^*$  formation. Moreover, the Bader charge density was further introduced to analyze that charge transfer occurred between the Fe atom and adsorbed  $\text{H}_2\text{O}_2$  (Fig. 5d). The results show that when  $\text{H}_2\text{O}_2$  was adsorbed on (4 0 0), (2 2 0) and (3 1 1) facets, the length of peroxy bond in  $\text{H}_2\text{O}_2$  increased by  $0.09$  Å,  $0.10$  Å and  $0.12$  Å,

respectively. And the charge density around the Fe atom decreased (blue area), while that around the O atom increased (yellow area). This was beneficial to the single-electron transfer process in the Haber-Weiss cycle [51], and further explains the phenomenon that the increase in the proportion of (3 1 1) facets will enhance the generation of  $\text{HO}^*$ .

### 3.4. Electrochemical properties of catalysts

Besides, the activation process of  $\text{H}_2\text{O}_2$  on the catalysts surface will also be influenced by the overall electrochemical properties of the catalysts. Afterwards, electrochemical spectroscopy of the catalysts was used to visualize the electron transfer in the Fenton-like process. The impedance data were fitted to the Randles circuit, and the Nyquist diagrams shown in Fig. 6a. The electric double layer capacitance ( $C_d$ ) of  $\text{Fe}_2\text{O}_3$  and  $\text{Fe}_2\text{O}_3$ -sheet were  $(20.63 \pm 0.52) \times 10^{-3} \mu\text{F}$  and  $(17.31 \pm 0.66) \times 10^{-3} \mu\text{F}$ , respectively, in which the higher  $C_d$  of  $\text{Fe}_2\text{O}_3$ -sheet

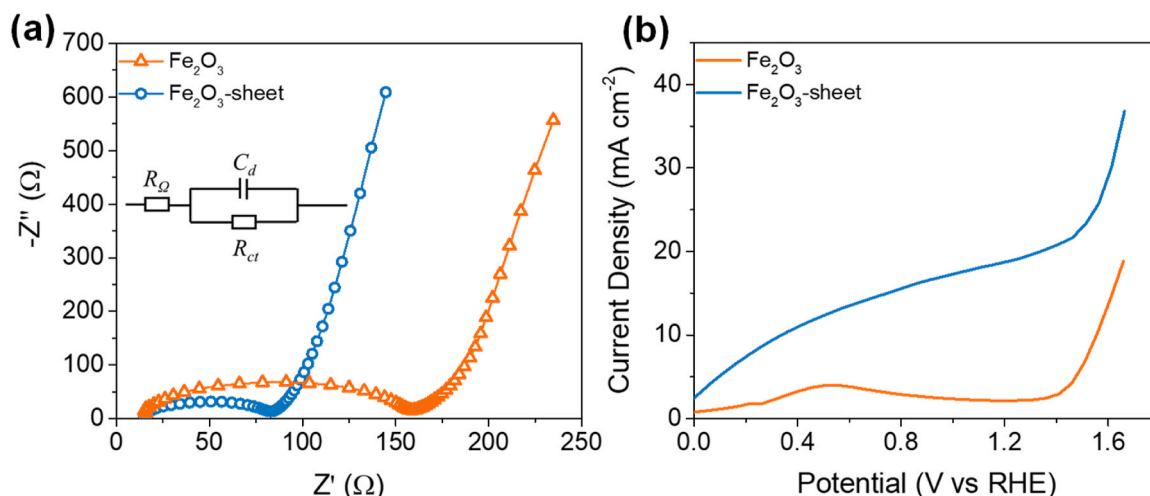


**Fig. 6.** (a) Electrochemical impedance spectroscopy and (b) linear sweep voltammetry of the ITO glass coated with  $\text{Fe}_2\text{O}_3$  and  $\text{Fe}_2\text{O}_3$ -sheet as the working electrode.



represents the stronger electron exchange properties [52]. It was conducive to the activation of  $\text{H}_2\text{O}_2$  on the  $\text{Fe}_2\text{O}_3$ -sheet surface. Moreover, electron transfer resistance ( $R_{ct}$ ) of the  $\text{Fe}_2\text{O}_3$ -sheet was  $71.3\ \Omega$  lower than that of  $\text{Fe}_2\text{O}_3$ . It will facilitate electron transfer inside the  $\text{Fe}_2\text{O}_3$ -sheet. Furthermore, the  $\text{Fe}_2\text{O}_3$ -sheet exhibits the highest current density of  $36.80\ \text{mA cm}^{-2}$  in contrast to  $18.82\ \text{mA cm}^{-2}$  of the  $\text{Fe}_2\text{O}_3$  (Fig. 6b), which confirming the high conductivity of the  $\text{Fe}_2\text{O}_3$ -sheet/ $\text{H}_2\text{O}_2$  system. This indicates that in addition to the iron sites with higher activity in  $\text{Fe}_2\text{O}_3$ -sheet, the efficient electron transfer process in  $\text{Fe}_2\text{O}_3$ -sheet/ $\text{H}_2\text{O}_2$  system will also promote  $\text{H}_2\text{O}_2$  activation.

Finally, the  $\text{Fe}_2\text{O}_3$ -sheet/ $\text{H}_2\text{O}_2$  still exhibited a stronger BPA degradation efficiency with lower Fe ion dissolution rate after 6 cycles (Fig. S14). This excluded the interference of homogeneous Fenton process. And it also maintains good structural stability in the Fenton-like process (Fig. S15).

#### 4. Conclusions

Increasing the production of  $\text{HO}^\bullet$  in Fenton-like process will improve the efficiencies of advanced purification of wastewater. The generation of  $\text{HO}^\bullet$  is closely related to the activation process of  $\text{H}_2\text{O}_2$  on the surface of the catalysts. However, structural features such as size, morphology and exposed facets will affect the screening of key factors of  $\text{H}_2\text{O}_2$  activation. In this work, we prepared an iron oxide nanosheet based on the ultrasonic-assisted method, normalized the difference of its physical structure, and explored the relationship between the exposed facets of the catalysts and the efficiency of  $\text{H}_2\text{O}_2$  activation. Wherein, the adsorption energy and activation energy of  $\text{H}_2\text{O}_2$  were the lowest on the (3 1 1) facet, which was conducive to the generation of  $\text{HO}^\bullet$  in the single electron transfer process. Moreover,  $\text{O}_2^\bullet$  adsorbed on (3 1 1) facet can be used as a precursor to generate the first-excited-state  $^1\text{O}_2$  through the orbital electron hybridization process. In addition, the nanosheet structure and good electrochemical properties of the  $\text{Fe}_2\text{O}_3$ -sheet can enhance the electron transfer efficiency in the Fenton-like system, and further promoting the formation of  $\text{HO}^\bullet$ . Substantially, this study provides a more comprehensive view on the mechanism of Fenton-like reaction mediated by different facets, and will facilitate the design of efficient Fenton-like catalysts in wastewater treatment.

#### CRedit authorship contribution statement

Yue Yin: Conceptualization, Investigation, Formal analysis, Writing - original draft & editing. Yake Zhang: Investigation, Methodology. Bo Wu: Formal analysis. Limin Hu: Investigation. Yan Wang: Resources. Junfeng Wan: Supervision, Resources, Validation, Writing - review. Weiming Zhang: Conceptualization, Supervision, Resources, Validation, Writing - review & editing.

#### Declaration of Competing Interest

We declare that we have no financial and personal relationships with other people or organizations that could have appeared to influence the work reported in this paper.

#### Data Availability

The data that has been used is confidential.

#### Acknowledgements

This study was financially supported by Natural Science Foundation of China (Grant No. 22176088 and 22206173) and China Postdoctoral Science Foundation (Grant No. 2022TQ0294).

#### Appendix A. Supporting information

Supplementary data associated with this article can be found in the online version at doi:10.1016/j.apcatb.2023.123165.

#### References

- [1] K. Fedorov, K. Dinesh, X. Sun, R. Darvishi Cheshmeh Soltani, Z. Wang, S. Sonawane, G. Boczkaj, Synergistic effects of hybrid advanced oxidation processes (AOPs) based on hydrodynamic cavitation phenomenon – a review, *Chem. Eng. J.* 432 (2022), 134191, <https://doi.org/10.1016/j.cej.2021.134191>.
- [2] Z. Yang, C. Shan, B. Pan, J.J. Pignatello, The fenton reaction in water assisted by picolinic acid: accelerated iron cycling and co-generation of a selective fe-based oxidant, *Environ. Sci. Technol.* 55 (2021) 8299–8308, <https://doi.org/10.1021/acs.est.1c00230>.
- [3] S. Patnaik, K.K. Das, A. Mohanty, K. Parida, Enhanced photo catalytic reduction of Cr(VI) over polymer-sensitized g-C<sub>3</sub>N<sub>4</sub>/ZnFe<sub>2</sub>O<sub>4</sub> and its synergism with phenol oxidation under visible light irradiation, *Catal. Today* 315 (2018) 52–66, <https://doi.org/10.1016/j.cattod.2018.04.008>.
- [4] Y. Chen, C.J. Miller, T.D. Waite, pH Dependence of hydroxyl radical, ferryl, and/or ferric peroxo species generation in the heterogeneous fenton process, *Environ. Sci. Technol.* 56 (2022) 1278–1288, <https://doi.org/10.1021/acs.est.1c05722>.
- [5] K.K. Das, S. Patnaik, B. Nanda, A.C. Pradhan, K. Parida, ZnFe<sub>2</sub>O<sub>4</sub>-decorated mesoporous Al<sub>2</sub>O<sub>3</sub> modified MCM-41: a solar-light-active photocatalyst for the effective removal of phenol and Cr(VI) from water, *ChemistrySelect* 4 (2019) 1806–1819, <https://doi.org/10.1002/slct.201803209>.
- [6] E. Gualda-Alonso, P. Soriano-Molina, J.L. García Sánchez, J.L. Casas López, J. A. Sánchez Pérez, Mechanistic modeling of solar photo-Fenton with Fe<sup>3+</sup>-NTA for microcontaminant removal, *Appl. Catal. B-Environ.* 318 (2022), 121795, <https://doi.org/10.1016/j.apcatb.2022.121795>.
- [7] Y. Gao, W. Zhu, J. Liu, P. Lin, J. Zhang, T. Huang, K. Liu, Mesoporous sulfur-doped CoFe<sub>2</sub>O<sub>4</sub> as a new Fenton catalyst for the highly efficient pollutants removal, *Appl. Catal. B-Environ.* 295 (2021), 120273, <https://doi.org/10.1016/j.apcatb.2021.120273>.
- [8] Y. Yin, Y. Ren, J. Lu, W. Zhang, C. Shan, M. Hua, L. Lv, B. Pan, The nature and catalytic reactivity of UiO-66 supported Fe<sub>3</sub>O<sub>4</sub> nanoparticles provide new insights into Fe-Zr dual active centers in Fenton-like reactions, *Appl. Catal. B-Environ.* 286 (2021), 119943, <https://doi.org/10.1016/j.apcatb.2021.119943>.
- [9] H. Li, J. Li, Z. Ai, F. Jia, L. Zhang, Oxygen vacancy-mediated photocatalysis of BiOCl: reactivity, selectivity, and perspectives, *Angew. Chem. Int. Ed.* 57 (2018) 122–138, <https://doi.org/10.1002/anie.201705628>.
- [10] Y. Zhao, F. Pan, H. Li, T. Niu, G. Xu, W. Chen, Facile synthesis of uniform  $\alpha$ -Fe<sub>2</sub>O<sub>3</sub> crystals and their facet-dependent catalytic performance in the photo-Fenton reaction, *J. Mater. Chem. A* 1 (2013) 7242–7246, <https://doi.org/10.1039/C3TA10966F>.
- [11] H. Jin, X. Tian, Y. Nie, Z. Zhou, C. Yang, Y. Li, L. Lu, Oxygen vacancy promoted heterogeneous fenton-like degradation of ofloxacin at pH 3.2–9.0 by Cu substituted magnetic Fe<sub>3</sub>O<sub>4</sub>@FeOOH nanocomposite, *Environ. Sci. Technol.* 51 (2017) 12699–12706, <https://doi.org/10.1021/acs.est.7b04503>.
- [12] K.K. Das, S. Mansingh, R. Mohanty, D.P. Sahoo, N. Priyadarshini, K. Parida, 0D–2D Fe<sub>2</sub>O<sub>3</sub>/boron-doped g-C<sub>3</sub>N<sub>4</sub> S-scheme exciton engineering for photocatalytic H<sub>2</sub>O<sub>2</sub> production and photo-fenton recalcitrant-pollutant detoxification: kinetics, influencing factors, and mechanism, *J. Phys. Chem. C* 127 (2023) 22–40, <https://doi.org/10.1021/acs.jpcc.2c06369>.
- [13] Y. Yin, R. Lv, W. Zhang, J. Lu, Y. Ren, X. Li, L. Lv, M. Hua, B. Pan, Exploring mechanisms of different active species formation in heterogeneous Fenton systems by regulating iron chemical environment, *Appl. Catal. B-Environ.* 295 (2021), 120282, <https://doi.org/10.1016/j.apcatb.2021.120282>.
- [14] S. Yang, H. He, D. Wu, D. Chen, X. Liang, Z. Qin, M. Fan, J. Zhu, P. Yuan, Decolorization of methylene blue by heterogeneous Fenton reaction using Fe<sub>3-x</sub>Ti<sub>x</sub>O<sub>4</sub> (0 ≤ x ≤ 0.78) at neutral pH values, *Appl. Catal. B-Environ.* 89 (2009) 527–535, <https://doi.org/10.1016/j.apcatb.2009.01.012>.
- [15] H.H. Kim, H. Lee, D. Lee, Y.J. Ko, H. Woo, J. Lee, C. Lee, A.L.T. Pham, Activation of hydrogen peroxide by a titanium oxide-supported iron catalyst: evidence for surface Fe(IV) and its selectivity, *Environ. Sci. Technol.* 54 (2020) 15424–15432, <https://doi.org/10.1021/acs.est.0c04262>.
- [16] J. Wang, K.P. Hou, Y. Wen, H. Liu, H. Wang, K. Chakarawet, M. Gong, X. Yang, Interlayer structure manipulation of iron oxychloride by potassium cation intercalation to steer H<sub>2</sub>O<sub>2</sub> activation pathway, *J. Am. Chem. Soc.* 144 (2022) 4294–4299, <https://doi.org/10.1021/jacs.1c12398>.
- [17] X.J. Yang, X.M. Xu, J. Xu, Y.F. Han, Iron oxychloride (FeOCl): an efficient fenton-like catalyst for producing hydroxyl radicals in degradation of organic contaminants, *J. Am. Chem. Soc.* 135 (2013) 16058–16061, <https://doi.org/10.1021/ja409130c>.
- [18] D.K. Padhi, T.K. Panigrahi, K. Parida, S.K. Singh, P.M. Mishra, Green synthesis of Fe<sub>3</sub>O<sub>4</sub>/RGO nanocomposite with enhanced photocatalytic performance for Cr(VI) reduction, phenol degradation, and antibacterial activity, *ACS Sustain. Chem. Eng.* 5 (2017) 10551–10562, <https://doi.org/10.1021/acsuschemeng.7b02548>.
- [19] R. Gao, L. Pan, Z. Li, C. Shi, Y. Yao, X. Zhang, J.J. Zou, Engineering facets and oxygen vacancies over hematite single crystal for intensified electrocatalytic H<sub>2</sub>O<sub>2</sub> production, *Adv. Funct. Mater.* 30 (2020) 1910539, <https://doi.org/10.1002/adfm.201910539>.

- [20] J. Qu, Y. Wang, X. Mu, J. Hu, B. Zeng, Y. Lu, M. Sui, R. Li, C. Li, Determination of crystallographic orientation and exposed facets of titanium oxide nanocrystals, *Adv. Mater.* 34 (2022) 2203320, <https://doi.org/10.1002/adma.202203320>.
- [21] M. Shi, G. Li, J. Li, X. Jin, X. Tao, B. Zeng, E.A. Pidko, R. Li, C. Li, Intrinsic facet-dependent reactivity of well-defined BiOBr nanosheets on photocatalytic water splitting, *Angew. Chem. Int. Ed.* 59 (2020) 6590–6595, <https://doi.org/10.1002/anie.201916510>.
- [22] C. Dai, X. Tian, Y. Nie, H.-M. Lin, C. Yang, B. Han, Y. Wang, Surface facet of CuFeO<sub>2</sub> nanocatalyst: a key parameter for H<sub>2</sub>O<sub>2</sub> activation in fenton-like reaction and organic pollutant degradation, *Environ. Sci. Technol.* 52 (2018) 6518–6525, <https://doi.org/10.1021/acs.est.8b01448>.
- [23] J.Y.T. Chan, S.Y. Ang, E.Y. Ye, M. Sullivan, J. Zhang, M. Lin, Heterogeneous photo-Fenton reaction on hematite ( $\alpha$ -Fe<sub>2</sub>O<sub>3</sub>)<sup>1</sup>, <sup>1</sup> and <sup>2</sup> surface facets, *Phys. Chem. Chem. Phys.* 17 (2015) 25333–25341, <https://doi.org/10.1039/C5CP03332B>.
- [24] M.D. Jiang, J.H. Lu, Y.F. Ji, D.Y. Kong, Bicarbonate-activated persulfate oxidation of acetaminophen, *Water Res.* 116 (2017) 324–331, <https://doi.org/10.1016/j.watres.2017.03.043>.
- [25] G.G. Kresse, J.J. Furthmüller, Efficient iterative schemes for ab initio total-energy calculations using a plane-wave basis set, *Phys. Rev. B* 54 (1996) 11169, <https://doi.org/10.1103/PhysRevB.54.11169>.
- [26] P. Blochl, E. Blochl, P. Blochl, Projected augmented-wave method, *Phys. Rev. B* 50 (1994) 17953, <https://doi.org/10.1103/physrevb.50.17953>.
- [27] J.P. Perdew, K. Burke, M. Ernzerhof, Generalized gradient approximation made simple, *Phys. Rev. Lett.* 77 (1996) 3865, <https://doi.org/10.1103/PhysRevLett.77.3865>.
- [28] A. Jain, S.P. Ong, G. Hautier, W. Chen, K.A. Persson, Commentary: the materials project: a materials genome approach to accelerating materials innovation, *APL Mater.* 1 (2013), 011002, <https://doi.org/10.1063/1.4812323>.
- [29] K. Sobańska, P. Pietrzyk, Z. Sojka, Generation of reactive oxygen species via electropotential interaction of H<sub>2</sub>O<sub>2</sub> with ZrO<sub>2</sub> gel: ionic sponge effect and pH-switchable peroxidase- and catalase-like activity, *ACS Catal.* 7 (2017) 2935–2947, <https://doi.org/10.1021/acscatal.7b00189>.
- [30] S. Zhang, M. Sun, T. Hedtke, A. Deshmukh, X. Zhou, S. Weon, M. Elimelech, J.-H. Kim, Mechanism of heterogeneous fenton reaction kinetics enhancement under nanoscale spatial confinement, *Environ. Sci. Technol.* 54 (2020) 10868–10875, <https://doi.org/10.1021/acs.est.0c02192>.
- [31] L. Chen, S. Wang, Z. Yang, J. Qian, B. Pan, Selective interfacial oxidation of organic pollutants in fenton-like system mediated by Fe(III)-adsorbed carbon nanotubes, *Appl. Catal. B-Environ.* 292 (2021), 120193, <https://doi.org/10.1016/j.apcatb.2021.120193>.
- [32] C.J. Miller, Y. Chang, C. Wegeberg, C.J. McKenzie, T.D. Waite, Kinetic analysis of H<sub>2</sub>O<sub>2</sub> activation by an Iron(III) complex in water reveals a nonhomolytic generation pathway to an Iron(IV)oxo complex, *ACS Catal.* 11 (2021) 787–799, <https://doi.org/10.1021/acscatal.0c02877>.
- [33] Z. Tang, P. Zhao, H. Wang, Y. Liu, W. Bu, Biomedicine meets Fenton chemistry, *Chem. Rev.* 121 (2021) 1981–2019, <https://doi.org/10.1021/acs.chemrev.0c00977>.
- [34] Z. Wang, J. Jiang, S.Y. Pang, Y. Zhou, C.T. Guan, Y. Gao, J. Li, Y. Yang, W. Qu, C. C. Jiang, Is sulfate radical really generated from peroxydisulfate activated by Iron (II) for environmental decontamination? *Environ. Sci. Technol.* 52 (2018) 11276–11284, <https://doi.org/10.1021/acs.est.8b02266>.
- [35] Y. Yang, G. Banerjee, G.W. Brudvig, J.H. Kim, J.J. Pignatello, Oxidation of organic compounds in water by unactivated peroxymonosulfate, *Environ. Sci. Technol.* 52 (2018) 5911–5919, <https://doi.org/10.1021/acs.est.8b00735>.
- [36] Q.X. Zhou, W.H. Lei, J.R. Chen, C. Li, Y.J. Hou, X.S. Wang, B.W. Zhang, A new heteroleptic ruthenium(II) polypyridyl complex with long-wavelength absorption and high singlet-oxygen quantum yield, *Chem. Eur. J.* 16 (2010) 3157–3165, <https://doi.org/10.1002/chem.200902563>.
- [37] P. Mulder, R. Louw, Kinetic H/D isotope effects for gas phase hydroxylation of benzene and chlorobenzene between 520–1080 K. Hydroxyl radical versus O(<sup>3</sup>P) atom attack, *Int. J. Chem. Kinet.* 20 (1988) 577–592, <https://doi.org/10.1002/kin.550200707>.
- [38] H. Gallard, L.J. De, Kinetics of oxidation of chlorobenzenes and phenyl-ureas by Fe(II)/H<sub>2</sub>O<sub>2</sub> and Fe(III)/H<sub>2</sub>O<sub>2</sub>. Evidence of reduction and oxidation reactions of intermediates by Fe(II) or Fe(III), *Chemosphere* 42 (2001) 405–413, [https://doi.org/10.1016/S0045-6535\(00\)00076-X](https://doi.org/10.1016/S0045-6535(00)00076-X).
- [39] D. Schröder, S. Bärsch, H. Schwarz, Second ionization energies of gaseous iron oxides and hydroxides: the FeO<sub>m</sub>H<sub>2</sub><sup>+</sup> dications (m = 1, 2; n ≤ 4)<sup>†</sup>, *J. Phys. Chem. A* 104 (2000) 5101–5110, <https://doi.org/10.1021/jp994389s>.
- [40] J.D.L. And, H. Gallard, Catalytic decomposition of hydrogen peroxide by Fe(III) in homogeneous aqueous solution: mechanism and kinetic modeling, *Environ. Sci. Technol.* 33 (1999) 2726–2732, <https://doi.org/10.1021/es981171v>.
- [41] C. Luo, M. Sadhasivan, J. Kim, V.K. Sharma, C.H. Huang, Revelation of Fe(V)/Fe(IV) involvement in the Fe(VI)–ABTS system: kinetic modeling and product analysis, *Environ. Sci. Technol.* 55 (2021) 3976–3987, <https://doi.org/10.1021/acs.est.0c07792>.
- [42] Y. Bu, H. Li, W. Yu, Y. Pan, L. Li, Y. Wang, L. Pu, J. Ding, G. Gao, B. Pan, Peroxydisulfate activation and singlet oxygen generation by oxygen vacancy for degradation of contaminants, *Environ. Sci. Technol.* 55 (2021) 2110–2120, <https://doi.org/10.1021/acs.est.0c07274>.
- [43] K.K. Das, S. Mansingh, D.P. Sahoo, R. Mohanty, K. Parida, Engineering an oxygen-vacancy-mediated step-scheme charge carrier dynamic coupling WO<sub>3-x</sub>/ZnFe<sub>2</sub>O<sub>4</sub> heterojunction for robust photo-Fenton-driven levofloxacin detoxification, *N. J. Chem.* 46 (2022) 5785–5798, <https://doi.org/10.1039/D2NJ00067A>.
- [44] K.K. Das, D.P. Sahoo, S. Mansingh, K. Parida, ZnFe<sub>2</sub>O<sub>4</sub>@WO<sub>3-x</sub>/polypyrrole: an efficient ternary photocatalytic system for energy and environmental application, *ACS Omega* 6 (2021) 30401–30418, <https://doi.org/10.1021/acsomega.1c03705>.
- [45] M. Lal, R. Rao, X. Fang, H.P. Schuchmann, C.V. Sonntag, Radical-induced oxidation of dithiothreitol in acidic oxygenated aqueous solution: a chain reaction, *J. Am. Chem. Soc.* 119 (1997) 5735–5739, <https://doi.org/10.1021/ja970744l>.
- [46] B. Bielski, G.G. Shue, S. Bajuk, Reduction of nitro blue tetrazolium by CO<sup>2-</sup> and O<sup>2-</sup> radicals, *Cheminform* 11 (1980) 830–833, <https://doi.org/10.1021/j100445a006>.
- [47] H. Zhang, W. Wang, H. Zhao, L. Zhao, L.-Y. Gan, L.H. Guo, Facet-dependent interfacial charge transfer in Fe(III)-grafted TiO<sub>2</sub> nanostructures activated by visible light, *ACS Catal.* 8 (2018) 9399–9407, <https://doi.org/10.1021/acscatal.8b02075>.
- [48] L. Notini, D.E. Latta, A. Neumann, C.I. Pearce, M. Sassi, A.T. N'Diaye, K.M. Rosso, M.M. Scherer, The role of defects in Fe(II)–goethite electron transfer, *Environ. Sci. Technol.* 52 (2018) 2751–2759, <https://doi.org/10.1021/acs.est.7b05772>.
- [49] J. Huang, A. Jones, T.D. Waite, Y. Chen, H. Zhang, Fe(II) redox chemistry in the environment, *Chem. Rev.* 121 (2021) 8161–8233, <https://doi.org/10.1021/acs.chemrev.0c01286>.
- [50] M. Yoshikiyo, K. Yamada, A. Namai, S.I. Ohkoshi, Study of the electronic structure and magnetic properties of ε-Fe<sub>2</sub>O<sub>3</sub> by first-principles calculation and molecular orbital calculations, *J. Phys. Chem. C* 116 (2012) 8688–8691, <https://doi.org/10.1021/jp300769z>.
- [51] L. Su, P. Wang, X. Ma, J. Wang, S. Zhan, Regulating local electron density of iron single sites by introducing nitrogen vacancies for efficient photo-fenton process, *Angew. Chem. Int. Ed.* 60 (2021) 21261–21266, <https://doi.org/10.1002/ange.202108937>.
- [52] P. Vadhva, J. Hu, M.J. Johnson, R. Stocker, M. Braglia, D.J.L. Brett, A.J.E. Rettie, Electrochemical impedance spectroscopy for all-solid-state batteries: theory, methods and future outlook, *ChemElectroChem* 8 (2021) 1930–1947, <https://doi.org/10.1002/celec.202100108>.